Unstable waves on a curved non-Newtonian liquid jet

2010 J. Phys. A: Math. Theor. 43 055501

(http://iopscience.iop.org/1751-8121/43/5/055501)

IOP PUBLISHING JOURNAL OF PHYSICS A: MATHEMATICAL AND THEORETICAL

J. Phys. A: Math. Theor. **43** (2010) 055501 (18pp) doi:10.1088/1751-8113/43/5/055501

Unstable waves on a curved non-Newtonian liquid jet

V L Hawkins[1], C J Gurney[2], S P Decent[2], M J H Simmons[1] and J Uddin[2]

[1] School of Chemical Engineering, University of Birmingham, Edgbaston, Birmingham, B15 2TT, UK
[2] School of Mathematics, University of Birmingham, Edgbaston, Birmingham, B15 2TT, UK

E-mail: S.P.Decent@bham.ac.uk

Received 15 September 2009, in final form 4 December 2009
Published 14 January 2010
Online at stacks.iop.org/JPhysA/43/055501

Abstract
A spiralling slender non-Newtonian liquid jet emerging from a rapidly rotating orifice is examined. The effect of the non-Newtonian rheology on the trajectory of the jet and its linear instability are determined using a mixture of computational and asymptotic methods. The sizes of the droplets produced by this instability are determined by considering the most unstable wave mode. This enables a quantitative comparison between theoretical and experimental results to be made, by comparing droplet sizes predicted from the theory with experimental measurements. At lower Weber numbers some good points of agreement have been obtained. At higher Weber numbers jet break-up becomes increasingly complex and the possibility of break-up being due to absolute, rather than convective, instability is discussed.

PACS number: 47.50.−d

1. Introduction

Curved liquid jets are relevant to the *prilling* process, which is widely used in industry to create small spherical pellets from molten material in many applications, such as the manufacture of fertilizer (urea), aluminium and magnesium pellets [1, 2]. In this process, molten liquid is pumped into a perforated vertical cylindrical drum suspended at the top of a cooling tower. As the drum rotates about its vertical axis, the liquid is flung outwards towards the drum wall and thousands of long curved jets are produced from the perforations on its surface. These break up due to the growth of capillary instabilities on the surface of the jets and the droplets produced fall against a counter current of cool air and solidify to form pellets. There are numerous economic reasons to control this instability process, to produce pellets of uniform size and suppress the formation of fine particles.

In Wallwork *et al* [3] asymptotic and numerical results were presented for an unstable inviscid liquid jet emerging from a rapidly rotating drum. This work was extended in Decent

et al [4] to include the effects of Newtonian viscosity. It was found that the trajectory and steady state of a liquid jet emerging from a rotating drum is only slightly affected by viscosity, but the instability process was dominated by viscosity and surface tension. Good agreement was obtained between theory and experimental data.

In the industrial context, the processing of non-Newtonian fluids is common. In a non-Newtonian fluid, the relation between the shear stress and the strain rate is nonlinear, and can also be time-dependent. The addition of polymers or immiscible phases creates liquid mixtures with non-Newtonian flow properties. Paints, slurries and polymer solutions are all examples which are ubiquitous in the industrial environment.

Despite obvious industrial interest, studies of the break-up of non-Newtonian jets are comparatively sparse when compared to the myriad of literature available on Newtonian jets. The focus of the majority of studies is on straight liquid jets, that being an axially symmetric flow with the jet having a circular cross-section at every point along its length, and both time-dependent (viscoelastic) and time-independent fluids have been considered. Work on viscoelastic materials (mostly polymer solutions) has elucidated some interesting features, notably the more rapid growth of nonlinear surface tension driven deformations, yet a retardation of the break-up of viscoelastic filaments due to extensional stresses [5]. This leads to the classic 'beads on a string' jet shape which has been studied in depth by e.g. Li and Fontelos [6] and Clasen *et al* [7]. A review of this area is given by McKinley [8].

A number of straight jet studies have investigated the behaviour of time-independent shear thinning or shear-thickening fluids; models have been developed assuming a power or Carreau constitutive law. Doshi *et al* [9] performed asymptotic solutions of the governing equations and showed that the effects of inertia become increasingly dominant as the point of pinch-off is reached, as found for Newtonian fluids [10]. Dravid *et al* [11] found good agreement between these models and experiments at low Reynolds numbers.

A number of authors have investigated the instability of non-Newtonian fluids with power-law rheology for classical problems, including flow down an inclined plane [12, 13], between concentric cylinders [14] as well as gravity driven shear flows [15].

Two recent studies examine the break-up of curved jets assuming a power-law dependence of the fluid rheology. Uddin *et al* [16] performed a linear asymptotic analysis and produced simulations for both shear thinning and shear thickening dependences, assuming that the unstable waves are long. Later work produced a nonlinear model for long waves [17], which enabled prediction of drop size and jet shape as well as the break-up length, which could also be obtained from the earlier linear analysis.

In this paper, we firstly determine the influence of non-Newtonian effects on the trajectory of our curved liquid jets, and then apply the methods of Rayleigh [18] and Weber [19] to determine their instability. The stability of the jet is analysed using spatial stability methods [20]. A series of experiments was also performed, to see how altering various parameters affects the trajectory, stability and droplet formation of the jet. Theoretical predictions are then compared to experimental results. The calculations presented here extend those of [16, 17] by making no assumption as to whether the waves are, in any sense, long or short, which gives rise to a more general dispersion relation.

2. The equations of motion

To model the prilling process a large circular cylindrical drum of radius s_0, rotating about its vertical axis of symmetry with angular velocity, Ω, is considered. A liquid jet emerges from a small circular orifice of radius a, situated on the curved surface of the cylinder.

The problem is examined by considering a co-ordinate system (x, y, z) which rotates with the drum. The origin of the co-ordinate system is chosen to be at the axis of the drum in line with the centre of the orifice. The orifice's centre is positioned at $(s_0, 0, 0)$ in this co-ordinate system, with the x-axis in the direction normal to the surface of the drum in the initial direction of the jet, and the z-axis orthogonal to the x-axis in the plane of the centreline of the jet. The positive z-axis points in the direction opposite to the motion of the drum. The y-axis points vertically upwards and is orientated in the direction opposite to gravitational acceleration.

The rotation of the jet causes the jet to curve on leaving the orifice and an analysis of the jet in the rotating (x, y, z) plane becomes difficult. Therefore, a curvilinear co-ordinate system, (s, n, ϕ), previously used by Wallwork *et al* [3], is used to describe the curved jet, where s is the arclength along the centreline of the jet, measured from the orifice, and (n, ϕ) are the plane polar co-ordinates in the radial and azimuthal directions in any cross-section of the jet. The origin of the co-ordinate system is at the centre of the circular cross-section of the jet. A diagram of the co-ordinate system can be found in [3]. The associated unit vectors are denoted by $\boldsymbol{e_s}$, $\boldsymbol{e_n}$ and $\boldsymbol{e_\phi}$, respectively.

The effects of gravity on the jet can be neglected if the centripetal acceleration of the jet, $s_0\Omega^2$, where Ω is the rotation of the drum (rad s^{-1}), is much greater than the acceleration due to gravity, g, acting in the negative y direction, as is the case with industrial prilling. Thus, the jet's centreline is assumed to lie solely in the x–z plane and the centreline of the jet is given by $(X(s,t) + s_0, 0, Z(s,t))$ in Cartesian co-ordinates, where t is the time and X and Z are functions to be found.

Non-dimensional equations are derived as in Uddin *et al* [16], using the transformations

$$\begin{aligned} &\bar{u} = \frac{u}{U}, \quad \bar{v} = \frac{v}{U}, \quad \bar{w} = \frac{w}{U}, \quad \bar{p} = \frac{p}{\rho U^2}, \quad \bar{n} = \frac{n}{a}, \quad \epsilon = \frac{a}{s_0}, \\ &\bar{R} = \frac{R}{a}, \quad \bar{s} = \frac{s}{s_0}, \quad \bar{t} = \frac{tU}{s_0}, \quad \bar{X} = \frac{X}{s_0}, \quad \bar{Z} = \frac{Z}{s_0}, \quad \bar{\eta} = \frac{\eta}{k}, \end{aligned} \tag{2.1}$$

where U is the exit speed of the jet in the rotating frame, ρ is the liquid density, ϵ is a small aspect ratio, p is the pressure, R is the jet radius, k (Pa s^α) is the fluid consistency index, and u, v and w are the tangential, radial and azimuthal velocity components relative to the centreline of the jet, respectively. The bars denote dimensionless quantities in the above expressions.

For power-law fluids

$$\boldsymbol{\tau} = \eta(\boldsymbol{\nabla u} + (\boldsymbol{\nabla u})^T) = \eta\boldsymbol{\gamma}, \tag{2.2}$$

where $\boldsymbol{\nabla u}$ is the velocity gradient tensor, the transpose of which is $(\boldsymbol{\nabla u})^T$, $\boldsymbol{\tau}$ is the stress tensor, $\boldsymbol{\gamma}$ is the rate of strain tensor and η is the apparent (effective) viscosity and is a function of shear rate, $\dot{\gamma}$, such that

$$\eta = k\dot{\gamma}^{\alpha-1}, \tag{2.3}$$

where α is the flow index number and is dimensionless. Fluids which follow such a model are deemed shear thickening or shear thinning depending on whether α is greater than, or less than unity. In the special case when $\alpha = 1, k = \eta$ and the Newtonian fluid is recovered. The shear rate is given by the second invariant of the rate of strain tensor:

$$\dot{\gamma} = \sqrt{\frac{\boldsymbol{\gamma} : \boldsymbol{\gamma}}{2}}. \tag{2.4}$$

From (2.2), we have that $\tau_{ij} = \eta\gamma_{ij}$. It is possible to evaluate the nine stress components and an expression for η can be obtained by using the expressions for γ_{ij}, such that

$$\eta = k \sum_{ij} \frac{\gamma_{ij}\gamma_{ij}}{2}^{\frac{\alpha-1}{2}}. \tag{2.5}$$

The flow is described using the velocity vector $\boldsymbol{u} = u\boldsymbol{e}_s + v\boldsymbol{e}_n + w\boldsymbol{e}_\phi$. The overbars are dropped and we arrive at the equations of motion describing the dynamics of the jet as in Uddin *et al* [16]. These include the continuity equation, Navier–Stokes equations, and the kinematic condition, tangential and normal stress conditions on the jet's surface $n = R(s, \phi, t)$ in this co-ordinate system. The resulting non-dimensional equations of motion differ to those found in Decent *et al* [4] through the dynamic viscosity being replaced by η and the inclusion of derivatives of η. In [16], Uddin *et al* considered these equations using a long wavelength assumption that is not adopted here, so this paper presents a more general approach.

We also have an arclength condition which is

$$X_s^2 + Z_s^2 = 1 \tag{2.6}$$

and

$$v = w = 0 \qquad \text{on} \quad n = 0, \tag{2.7}$$

since on the centreline of the jet there is purely tangential flow.

3. Asymptotic form of the steady-state solutions

In Wallwork *et al* [3], an inviscid steady jet trajectory and steady expressions for the velocity, pressure and jet radius, based on a regular slender jet asymptotic expansion, using $0 < \epsilon \ll 1$, were obtained. This calculation was extended in Decent *et al* [4] to include Newtonian viscosity and is adapted here to include non-Newtonian power-law rheology.

The steady jet asymptotic expansions for u, v, p, R, X, Z from Wallwork *et al* [3] are applied, along with a steady jet expansion for η, the apparent viscosity; w is taken to be zero, so that there is no velocity component in the azimuthal direction. The expansions are

$$\begin{aligned}
\boldsymbol{u} &= \boldsymbol{u}_0(s) + \epsilon \boldsymbol{u}_1(s, n, \phi) + \mathrm{O}(\epsilon^2),\\
p &= p_0(s, n, \phi) + \epsilon p_1(s, n, \phi) + \mathrm{O}(\epsilon^2),\\
R &= R_0(s) + \epsilon R_1(s, \phi) + \mathrm{O}(\epsilon^2),\\
\boldsymbol{X} &= \boldsymbol{X}_0(s) + \epsilon \boldsymbol{X}_1(s, \phi) + \mathrm{O}(\epsilon^2),\\
\eta &= \eta_0(s) + \epsilon \eta_1(s, n, \phi) + \mathrm{O}(\epsilon^2),
\end{aligned} \tag{3.1}$$

where $\boldsymbol{u}_i = u_i\boldsymbol{e}_s + v_i\boldsymbol{e}_n$, $v_0 = 0$ and $\boldsymbol{X}_i = X_i\mathbf{i} + Z_i\mathbf{k}$ for $i = 0, 1, \ldots$. For simplicity of notation the leading-order components X_0 and Z_0 are rewritten as X and Z.

When this asymptotic expansion is considered, the expression for η is greatly simplified from (2.5), and can be expressed as

$$\begin{aligned}
\eta = k|\sqrt{3}u_{0s}|^{\alpha-1}\Bigg(1 + (\epsilon n)\frac{\alpha-1}{u_{0s}}\Bigg(\Bigg(u_0\Big(X_sZ_{ss} - Z_sX_{ss}\Big)\\
- \frac{u_{0s}}{2}\Big(X_sZ_{ss} - Z_sX_{ss}\Big)\Bigg)\cos\phi\Bigg) + O(\epsilon)^2\Bigg).
\end{aligned}$$

The leading-order equations are obtained for the steady flow as

$$n\frac{\mathrm{d}u_0}{\mathrm{d}s} + v_1 + n\frac{\partial v_1}{\partial n} = 0, \tag{3.2}$$

$$u_0\frac{\mathrm{d}u_0}{\mathrm{d}s} = -\frac{\partial p_0}{\partial s} + \frac{1}{Rb^2}((X+1)X_s + ZZ_s) + \frac{\eta_0}{\mathcal{R}e_\alpha}\left(\frac{1}{n}\frac{\partial u_1}{\partial n} + \frac{\partial^2 u_1}{\partial n^2} + \frac{1}{n^2}\frac{\partial^2 u_1}{\partial \phi^2}\right), \tag{3.3}$$

$$\frac{\partial p_0}{\partial n} = 0, \tag{3.4}$$

$$-\cos\phi(X_s Z_{ss} - Z_s X_{ss})u_0^2 = -\frac{\partial p_1}{\partial n} - \frac{2u_0\cos\phi}{Rb} + \frac{\cos\phi}{Rb^2}((X+1)Z_s - ZX_s) + \frac{\eta_0}{\mathcal{R}e_\alpha}\left(\frac{1}{n}\frac{\partial v_1}{\partial n} + \frac{\partial^2 v_1}{\partial n^2} + \frac{1}{n^2}\left(-v_1 + \frac{\partial^2 v_1}{\partial\phi^2}\right)\right), \tag{3.5}$$

$$\frac{\partial p_0}{\partial \phi} = 0, \tag{3.6}$$

$$\sin\phi(X_s Z_{ss} - Z_s X_{ss})u_0^2 = -\frac{1}{n}\frac{\partial p_1}{\partial\phi} + \frac{2u_0\sin\phi}{Rb} + \frac{\sin\phi}{Rb^2}(ZX_s - (X+1)Z_s) + \frac{\eta_0}{\mathcal{R}e_\alpha}\left(\frac{2}{n^2}\frac{\partial v_1}{\partial\phi}\right), \tag{3.7}$$

$$u_0\frac{\mathrm{d}R_0}{\mathrm{d}s} = v_1 \qquad \text{on} \quad n = R_0, \tag{3.8}$$

$$\frac{\partial u_1}{\partial n} = u_0\cos\phi(X_s Z_{ss} - Z_s X_{ss}) \qquad \text{on} \quad n = R_0, \tag{3.9}$$

$$p_0 = \frac{1}{nWe} \quad \text{on} \quad n = R_0, \tag{3.10}$$

$$p_1 - \frac{2\eta_0}{\mathcal{R}e_\alpha}\frac{\partial v_1}{\partial n} = \frac{1}{We}\left(-\frac{1}{R_0^2}\left(R_1 + \frac{\partial^2 R_1}{\partial\phi^2}\right) + \cos\phi(X_s Z_{ss} - Z_s X_{ss})\right) \quad \text{on} \quad n = R_0, \tag{3.11}$$

$$v_1 = 0 \qquad \text{on} \quad n = 0 \tag{3.12}$$

and

$$X_s^2 + Z_s^2 = 1. \tag{3.13}$$

The dimensionless parameters in these equations are the Weber number, $We = \rho U^2 a/\sigma$, the Rossby number, $Rb = U/(s_0\Omega)$, the aspect ratio, $\epsilon = a/s_0$ (which is chosen to be small as the asymptotics are based on this; this also corresponds to a slender jet) and the generalized Reynolds number, $\mathcal{R}e_\alpha = \epsilon(\rho/k)s_0^\alpha U^{2-\alpha} = \mathrm{O}(1)$. This scaling is necessary so that in the following section it is possible to obtain a distinguished limit in the resulting unstable equations.

On first inspection the above equations appear different to the leading-order equations for the inviscid case stated in Wallwork *et al* [3]. However, at leading-order these equations actually produce the same trajectory as in the inviscid case. Guided by Wallwork *et al* [3] and Decent *et al* [4], from the continuity equation (3.2) and (2.7), it is possible to obtain $v_1 = -\frac{n}{2}\frac{\mathrm{d}u_0}{\mathrm{d}s}$. Substituting this expression for v_1 into equations (3.5) and (3.7), it can be seen that the non-Newtonian terms on the right-hand sides of these equations become identically equal to zero. Therefore, apparent viscosity now only appears in (3.3) and in (3.11). Equation (3.3) can be rewritten as

$$f(s) = \nabla_{n,\phi}^2 u_1, \tag{3.14}$$

where

$$\nabla_{n,\phi}^2 = \frac{1}{n}\frac{\partial}{\partial n} + \frac{\partial^2}{\partial n^2} + \frac{1}{n^2}\frac{\partial^2}{\partial\phi^2}$$

is the in-plane Laplacian operator. Equations (3.4) and (3.6) imply that $p_0 = p_0(s)$. In (3.14),

$$f(s) = \frac{\mathcal{R}e_\alpha}{\eta_0}\left(u_0\frac{\mathrm{d}u_0}{\mathrm{d}s} + \frac{\mathrm{d}p_0}{\mathrm{d}s} - \frac{1}{Rb^2}((X+1)X_s + ZZ_s)\right).$$

Therefore, (3.14) has to be solved subject to (3.9). This is a Neumann problem on a circular domain, where s is a parameter. The method of Nayfeh [21] can be followed closely and a solvability argument can be used to analyse the problem. To determine a solvability condition, (3.14) is multiplied by $u(s, n, \phi)$ and the result is integrated over the domain of interest S ($0 \leqslant n \leqslant R_0$, $0 \leqslant \phi \leqslant 2\pi$), giving

$$\iint_S u\nabla^2_{n,\phi}u_1 \,\mathrm{d}S = \iint_S uf(s)\,\mathrm{d}S. \tag{3.15}$$

Now from Green's identity

$$\iint_S \left(u\nabla^2_{n,\phi}u_1 - u_1\nabla^2_{n,\phi}u\right)\,\mathrm{d}S = \int_B \left(u\frac{\partial u_1}{\partial n} - u_1\frac{\partial u}{\partial n}\right)\,\mathrm{d}B, \tag{3.16}$$

where B is the boundary of S (so that $n = R_0$ on B). Let u satisfy the homogeneous Neumann problem, so that

$$\nabla^2_{n,\phi}u = 0 \qquad \text{with} \qquad \frac{\partial u}{\partial n} = 0 \quad \text{on} \quad n = R_0, \tag{3.17}$$

while u_1 satisfies (3.14) subject to

$$\frac{\partial u_1}{\partial n} = g(s)\cos\phi \quad \text{on} \quad n = R_0, \tag{3.18}$$

where $g(s) = u_0\,(X_s Z_{ss} - X_{ss} Z_s)$. Therefore,

$$\iint_S u\nabla^2_{n,\phi}u_1 \,\mathrm{d}S = \int_B u\frac{\partial u_1}{\partial n}\,\mathrm{d}B. \tag{3.19}$$

From (3.15), (3.18) and (3.19) we obtain

$$\int_0^{2\pi}\int_0^{R_0} unf(s)\,\mathrm{d}n\,\mathrm{d}\phi = \int_0^{2\pi}\left[u\frac{\partial u_1}{\partial n}\right]_{n=R_0} R_0\,\mathrm{d}\phi = \int_0^{2\pi}[u]_{n=R_0}R_0 g(s)\cos\phi\,\mathrm{d}\phi. \tag{3.20}$$

The general solution to

$$\nabla^2_{n,\phi}u = 0$$

is given by

$$u = \beta(s)\phi + \sigma(s)ln(n) + \gamma(s) + \sum_{\lambda=1}^{\infty} n^{\lambda}(C_\lambda\cos(\lambda\phi) + D_\lambda\sin(\lambda\phi)). \tag{3.21}$$

The term $\beta(s)\phi$ is not periodic with 2π and $\sigma(s)ln(n)$ is singular at $n = 0$. Therefore, $\beta(s) = \sigma(s) = 0$ for all s. Consequently,

$$\left[\frac{\partial u}{\partial n}\right]_{n=R_0} = \sum_{\lambda=1}^{\infty}\lambda R_0^{\lambda-1}(C_\lambda\cos(\lambda\phi) + D_\lambda\sin(\lambda\phi)). \tag{3.22}$$

For u to satisfy the homogeneous problem (3.17), $C_\lambda = D_\lambda = 0$ for all λ. Therefore, the general solution to (3.14) which is bounded in $0 \leqslant n \leqslant R_0$ and also periodic in ϕ with period 2π is $u = \gamma(s)$ for some $\gamma(s)$. The left-hand side of (3.20) becomes

$$\gamma(s)f(s)\int_0^{2\pi}\int_0^{R_0} n\,\mathrm{d}n\,\mathrm{d}\phi = \gamma(s)f(s)\pi R_0^2, \tag{3.23}$$

and the right-hand side of (3.20) gives

$$\gamma(s)R_0 g(s)\int_0^{2\pi}\cos\phi\,\mathrm{d}\phi = 0. \tag{3.24}$$

Therefore, $\gamma(s)f(s)R_0^2 = 0$. Here, R_0 cannot be zero and since $u = \gamma(s)$ is the general solution to the homogeneous problem, we must have $f(s) = 0$ for all s (see Nayfeh [21]). Therefore, (3.3) and (3.9) give rise to two equations, namely $f(s) = 0$ and $\nabla^2_{n,\phi}u_1 = 0$. Neither of these expressions contain apparent viscosity.

Finally if we perform the calculation $\sin\phi(3.5) + \cos\phi(3.7)$, we obtain

$$\sin\phi\frac{\partial p_1}{\partial n} + \cos\phi\frac{1}{n}\frac{\partial p_1}{\partial \phi} = 0,$$

which has the solution $p_1 = n\cos\phi g_1(s) + h_1(s) + k_1(s)$, where $k_1(s)$ is the viscous part of p_1. Substituting this solution into (3.11) we obtain

$$R_0\cos\phi g_1(s) + h_1(s) + k_1(s) + \frac{\eta_0}{\mathcal{R}e_\alpha}\frac{\mathrm{d}u_0}{\mathrm{d}s} = \frac{1}{We}\left(-\frac{1}{R_0}\left(R_1 + \frac{\partial^2 R_1}{\partial\phi^2}\right) + \cos\phi\,(X_sZ_{ss} - X_{ss}Z_s)\right),$$

which has the solution $R_1 = g_2(s)\cos\phi + g_3(s)\sin\phi - h_1(s)WeR_0^2$ and $k_1(s) = -\frac{\eta_0}{\mathcal{R}e_\alpha}\frac{\mathrm{d}u_0}{\mathrm{d}s}$. Since R_1 must be periodic in ϕ with period 2π, it cannot have a particular solution of the form $\phi\sin\phi$. Therefore,

$$g_1 = \frac{1}{We}R_0\,(X_sZ_{ss} - X_{ss}Z_s)$$

and

$$p_1 = \frac{n}{WeR_0}\cos\phi\,(X_sZ_{ss} - X_{ss}Z_s) + h_1(s) - \frac{\eta_0}{\mathcal{R}e_\alpha}\frac{\mathrm{d}u_0}{\mathrm{d}s}, \tag{3.25}$$

where $h_1(s)$ could be found at next order in the asymptotic expansion. It should be noted that p_1 only appears as derivatives with respect to n and ϕ in equations (3.5) and (3.7). By substituting (3.25) into (3.5) and (3.7) no viscous contribution from p_1 is obtained since the viscous term in (3.25) in η_0 is dependent on s only. Therefore, the non-Newtonian terms vanish and the same leading-order problem for the trajectory is found here as in the inviscid case in Wallwork *et al* [3] along with the following leading-order equation for η_0:

$$\eta_0 = \left|\sqrt{3}\,\frac{\mathrm{d}u_0}{\mathrm{d}s}\right|^{\alpha-1}, \tag{3.26}$$

which gives the non-Newtonian component of the system. Hence, the apparent viscosity does not affect the steady solution at leading order, except in (3.26) and in a correction to p_1 in (3.25) which does not affect the trajectory, velocity, pressure or jet radius at leading order. This confirms the approach adopted in [16, 17] and Părău *et al* [22] also showed numerically that viscosity is not important to the trajectory except in very high viscosity liquids. The slender jet approximation in this case results in no shear across the jet at leading order.

4. Linear instability of the steady-state solutions

A linear stability analysis of the steady-state solutions is now performed using

$$\begin{aligned}
\boldsymbol{u} &= \bar{\boldsymbol{u}} + \delta\tilde{\boldsymbol{u}}(s,\bar{s},t,\bar{t},n,\phi),\\
p &= \bar{p} + \delta\tilde{p}(s,\bar{s},t,\bar{t},n,\phi),\\
R &= \bar{R} + \delta\tilde{R}(s,\bar{s},t,\bar{t},\phi),\\
\boldsymbol{X} &= \bar{\boldsymbol{X}} + \delta\epsilon\tilde{\boldsymbol{X}}(s,\bar{s},t,\bar{t}),\\
\eta &= \bar{\eta} + \delta\tilde{\eta}(s,\bar{s},t,\bar{t},n,\phi),
\end{aligned} \tag{4.1}$$

where $(\bar{\boldsymbol{u}}, \tilde{\boldsymbol{u}}) = (\bar{u}, \tilde{u})\boldsymbol{e}_s + (\bar{v}, \tilde{v})\boldsymbol{e}_n + (\bar{w}, \tilde{w})\boldsymbol{e}_\phi$, $(\bar{\boldsymbol{X}}, \tilde{\boldsymbol{X}}) = (\bar{X}, \tilde{X})\mathbf{i} + (\bar{Z}, \tilde{Z})\mathbf{k}$ and δ is a small dimensionless parameter, such that $0 < \delta \ll \epsilon \ll 1$, which measures the size of the unsteady disturbances as in Wallwork *et al* [3] (we note that we first tried $\boldsymbol{X} = \bar{\boldsymbol{X}} + \delta\widetilde{\boldsymbol{X}_0}(s, \bar{s}, t, \bar{t}) + \delta\epsilon\tilde{\boldsymbol{X}}(s, \bar{s}, t, \bar{t})$, but $\widetilde{\boldsymbol{X}_0}$ was found to be identically equal to zero). These linear perturbations disturb the basic steady solution (denoted by a quantity with an overbar in (4.1)), which are functions of s, n, ϕ, by unsteady quantities which are functions of s, $\bar{s}$, t, $\bar{t}$, n and ϕ, where $\bar{s} = \frac{s}{\epsilon}$ is a short lengthscale and $\bar{t} = \frac{t}{\epsilon}$ is a small timescale associated with short wave-like disturbances. The unsteady perturbations are denoted by variables with a tilde. Therefore, the small unsteady components allow motion on a short length scale which scales with the orifice a. These equations are substituted into the non-Newtonian equations of motion and linearized in the unsteady quantities (taking terms of $O(\delta)$). Having taken the leading-order equations in ϵ, we then look for solutions in modes of the form

$$\begin{aligned}
\tilde{\boldsymbol{u}} &= \hat{\boldsymbol{u}}(s, n, \phi, t)\exp(\mathrm{i}k(s)\bar{s} + \lambda(s)\bar{t}) + \text{c.c.},\\
\tilde{p} &= \hat{p}(s, n, \phi, t)\exp(\mathrm{i}k(s)\bar{s} + \lambda(s)\bar{t}) + \text{c.c.},\\
\tilde{R} &= \hat{R}(s, \phi, t)\exp(\mathrm{i}k(s)\bar{s} + \lambda(s)\bar{t}) + \text{c.c.},\\
\tilde{\boldsymbol{X}} &= \hat{\boldsymbol{X}}(s, t)\exp(\mathrm{i}k(s)\bar{s} + \lambda(s)\bar{t}) + \text{c.c.},
\end{aligned} \tag{4.2}$$

where $\hat{\boldsymbol{u}} = \hat{u}\mathbf{e_s} + \hat{v}\mathbf{e_n} + \hat{w}\mathbf{e}_\phi$, $\hat{\boldsymbol{X}} = \hat{X}\mathbf{i} + \hat{Z}\mathbf{k}$, c.c. denotes complex conjugate, $k(s)$ is the wavenumber and $\lambda(s)$ is the wave frequency. Looking for solutions by expanding the remaining unknowns (in the variables with 'hats') in Fourier series in ϕ, it is possible to find a countably infinite set of eigenvalue relationships, each associated with $\cos(n\phi)$ or $\sin(n\phi)$ for each integer n. After some lengthy algebra it can be determined that these are stable modes for $n \geqslant 1$, plus one unstable mode, corresponding to $n = 0$, which has the following eigenvalue relation:

$$\begin{aligned}
&-2\mathrm{i}k^5\eta_0 We I_1(\tilde{k}R_0)I_0(kR_0)R_0^2u_0 + k^5\mathcal{R}e_\alpha I_1(kR_0)I_1(\tilde{k}R_0)R_0^2\\
&\quad + k^4 We\mathcal{R}e_\alpha I_0(kR_0)I_1(\tilde{k}R_0)R_0^2u_0^2 - 2\mathrm{i}k^4\eta_0 We I_1(\tilde{k}R_0)I_1(kR_0)R_0u_0\\
&\quad - 2k^4\lambda\eta_0 We I_1(\tilde{k}R_0)I_0(kR_0)R_0^2 + 4\mathrm{i}k^4\tilde{k}\eta_0 We I_1(kR_0)I_0(\tilde{k}R_0)R_0^2u_0\\
&\quad + 4k^3\tilde{k}\lambda\eta_0 We I_1(kR_0)I_0(\tilde{k}R_0)R_0^2 - 2\mathrm{i}k^3\tilde{k}^2\eta_0 We I_1(\tilde{k}R_0)I_0(kR_0)R_0^2u_0\\
&\quad - k^3\mathcal{R}e_\alpha I_1(kR_0)I_1(\tilde{k}R_0) - 2\mathrm{i}k^3\lambda We\mathcal{R}e_\alpha I_0(kR_0)I_1(\tilde{k}R_0)R_0^2\\
&\quad - 2k^3\lambda\eta_0 We I_1(\tilde{k}R_0)I_1(kR_0)R_0 - k^3\tilde{k}^2\mathcal{R}e_\alpha I_1(kR_0)I_1(\tilde{k}R_0)R_0^2\\
&\quad - 2k^2\tilde{k}^2\lambda\eta_0 We I_1(\tilde{k}R_0)I_0(kR_0)R_0^2 + k^2\tilde{k}^2 We\mathcal{R}e_\alpha I_0(kR_0)I_1(\tilde{k}R_0)R_0^2u_0^2\\
&\quad - k^2\lambda^2 We\mathcal{R}e_\alpha I_0(kR_0)I_1(\tilde{k}R_0)R_0^2 + 2\mathrm{i}k^2\tilde{k}^2\eta_0 We I_1(\tilde{k}R_0)I_1(kR_0)R_0u_0\\
&\quad - 2\mathrm{i}k\tilde{k}^2\lambda We\mathcal{R}e_\alpha I_0(kR_0)I_1(\tilde{k}R_0)R_0^2u_0 + k\tilde{k}^2\mathcal{R}e_\alpha I_1(kR_0)I_1(\tilde{k}R_0)\\
&\quad + 2k\tilde{k}^2\lambda\eta_0 We I_1(\tilde{k}R_0)I_1(kR_0)R_0 - \tilde{k}^2\lambda^2 We\mathcal{R}e_\alpha I_0(kR_0)I_1(\tilde{k}R_0)R_0^2 = 0
\end{aligned} \tag{4.3}$$

where

$$\tilde{k} = \sqrt{k^2 + \frac{\mathcal{R}e_\alpha(\lambda + \mathrm{i}ku_0)}{\eta_0}}, \tag{4.4}$$

and I_n is the modified Bessel function of order n. Note for this mode $\tilde{w} = 0$. In this paper R_0 and u_0 are functions of arclength, s, and depend upon the rotation parameter Rb and satisfy the differential equations found in [3, 4]. This eigenvalue relationship can be interpreted in two different ways, using a temporal or spatial instability approach. Note that (4.3) reduces to the simpler result of Uddin *et al* [16] in the long wavelength limit $k \to 0$. Also (4.3) reduces to the classical straight jet Newtonian viscous result of [19] as $Rb \to \infty$ and $\alpha = 1$.

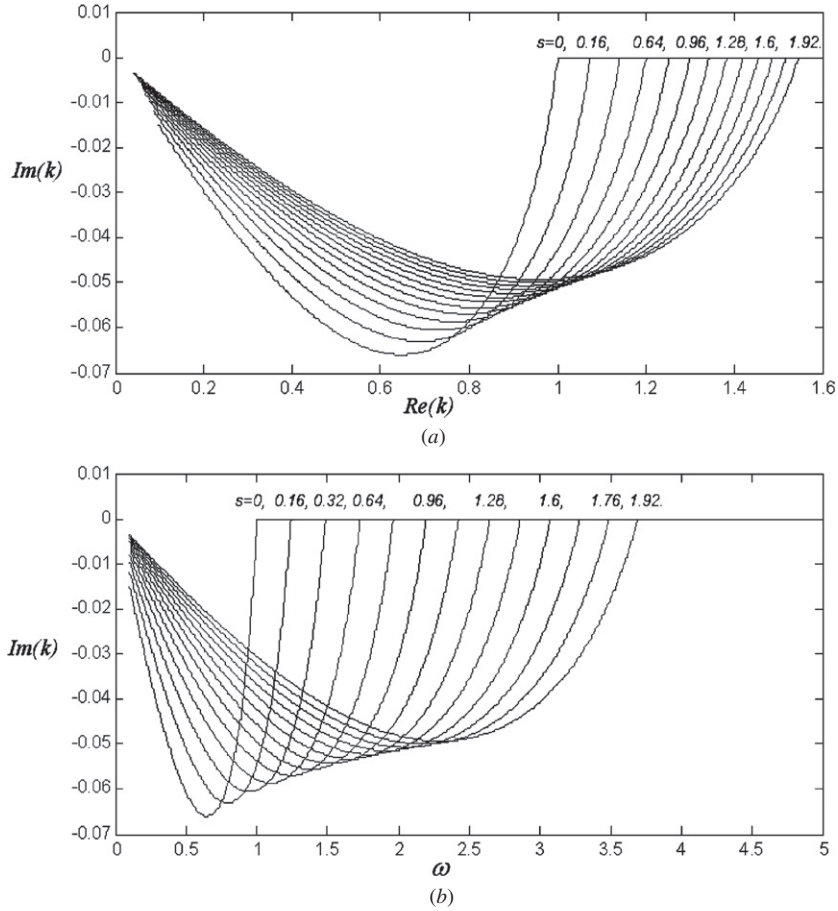

Figure 1. Graph showing (*a*) $Im(k)$ against $Re(k)$ and (*b*) $Im(k)$ against ω for various values of s ($We = 20$, $Rb = 1, \alpha = 0.8, \mathcal{R}e_\alpha = 40$).

5. Spatial instability

Following Keller *et al* [20], the eigenvalue relation is considered in terms of spatial instability. This was shown in [20] to be physically more realistic than temporal instability. An instability mode of the form $\exp(\mathrm{i}k(s)\bar{s} + \lambda(s)\bar{t})$ is considered, where k is complex, while $\lambda = -\mathrm{i}\omega$ is purely imaginary and ω is a real frequency. The eigenvalue relationship (4.3) is then solved for k, describing the wavenumber of the wave, $Re(k)$, and its spatial growth rate $-Im(k)$. The mode is unstable when $Im(k) < 0$. The largest growth rate, $Re(k) = k^*$, will correspond to the most negative value of $Im(k)$ and ω^* is the corresponding frequency.

The eigenvalue relationship (4.3) can be solved computationally. It can be shown graphically how the spatial mode varies for various values of the parameters. Figure 1 shows computational solutions to (4.3) at various values of s. In figure 1(*a*) each line of the graphs has been constructed by varying ω from 0 to 5. As s increases, it can be seen that the most unstable wave has a larger wavenumber, $Re(k)$, yielding shorter wavelength disturbances and a smaller growth rate, $Im(k)$. Figure 1(*b*) presents a graph of the growth rate, $Im(k)$, plotted

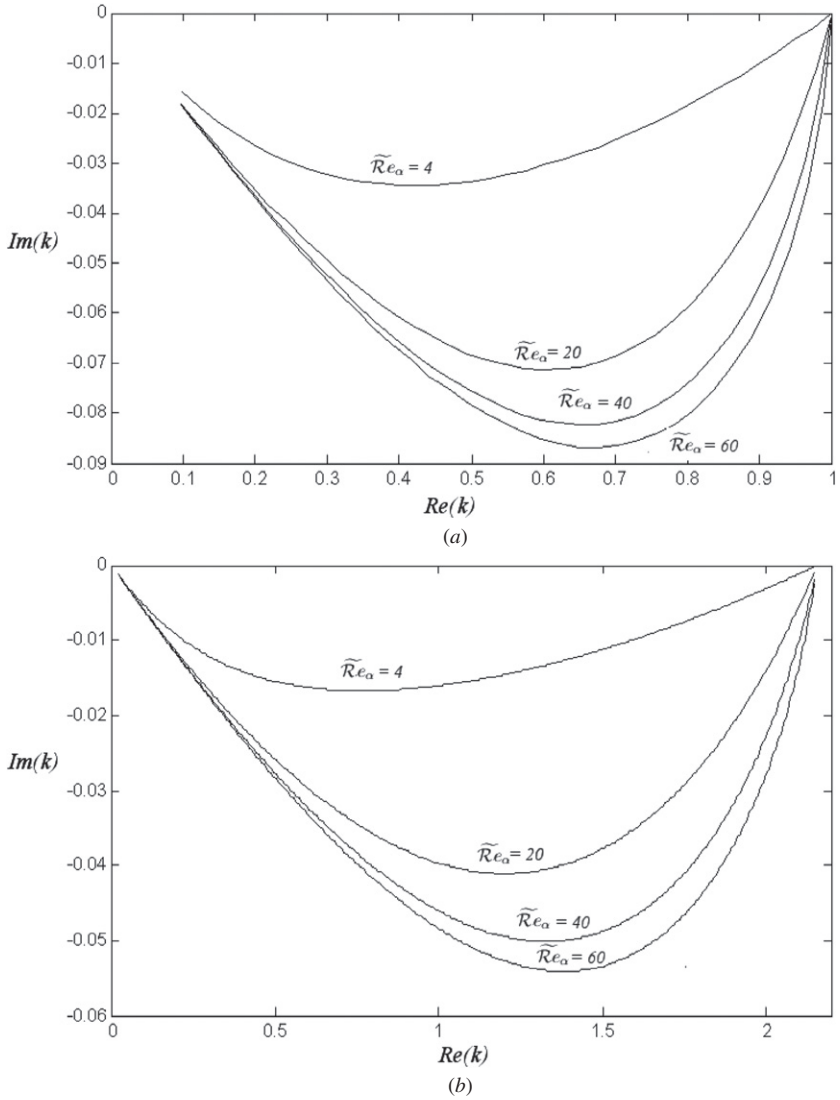

Figure 2. Graph showing $Im(k)$ against $Re(k)$ at (*a*) $s = 0$ and (*b*) $s = 10$, for various Reynolds numbers ($We = 13.33$, $Rb = 1.12$, $\alpha = 0.92$).

against the frequency, ω, for various parameters. The wavenumber with the largest growth rate occurs for higher values of ω for greater values of s.

Figures 2(*a*) and 2(*b*) show computational solutions to (4.3) at two different values of the arclength, s. The figures describe two different points on the jet and the most unstable mode on each curve occurs at the minimum value. Figures 2(*a*) and 2(*b*) show that decreasing the Reynolds number causes the jet to be less unstable as the waves are more heavily damped. For smaller Reynolds numbers, the most unstable wave occurs at longer wavelengths.

Figures 3(*a*) and 3(*b*) show that decreasing α causes the jet to become more unstable. For larger values of α, the most unstable wave occurs at longer wavelengths.

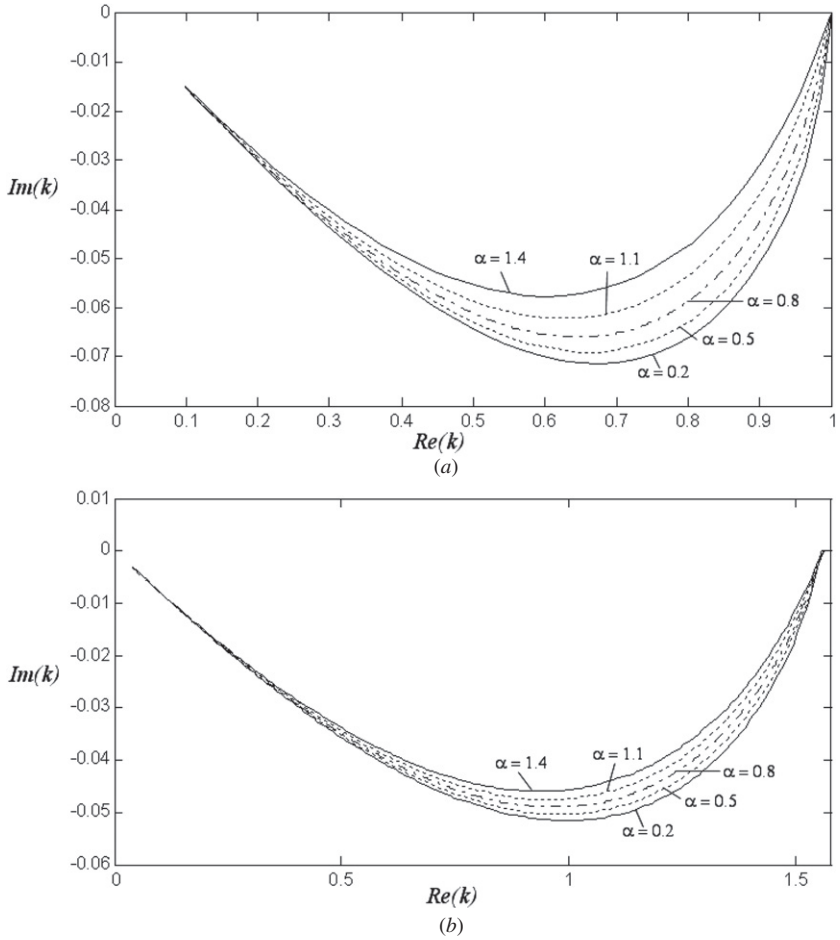

Figure 3. Graph showing $Im(k)$ against $Re(k)$ at (*a*) $s = 0$ and (*b*) $s = 10$, for various α ($\mathcal{R}e_\alpha = 40$, $We = 20$, $Rb = 1$).

Figures 4 and 5 show how the frequency of the most unstable mode, ω^*, associated with (4.3) and the growth rate, $|Im(k)|$, of the most unstable mode vary with Rossby number.

These graphs show the same trends as were found for a fluid of zero viscosity, that for decreasing Rossby number the values of frequency are larger and the growth rate of the most unstable mode reduces.

Temporal instability, which is physically less realistic [20], is considered in [23].

6. Comparison with experiments

The apparatus consists of a vertical cylindrical drum with a radius, $s_0 = 0.1425$ m and a height of 0.5 m (which is approximately 50% of the full industrial scale for fertilizer production at *Norsk Hydro* in Norway [24]), rotating about its vertical axis. The drum was filled with fluid to a height H, giving aspect ratios ($H/2s_0$) ranging from $\frac{1}{2}$ to $\frac{1}{4}$. A single orifice of variable

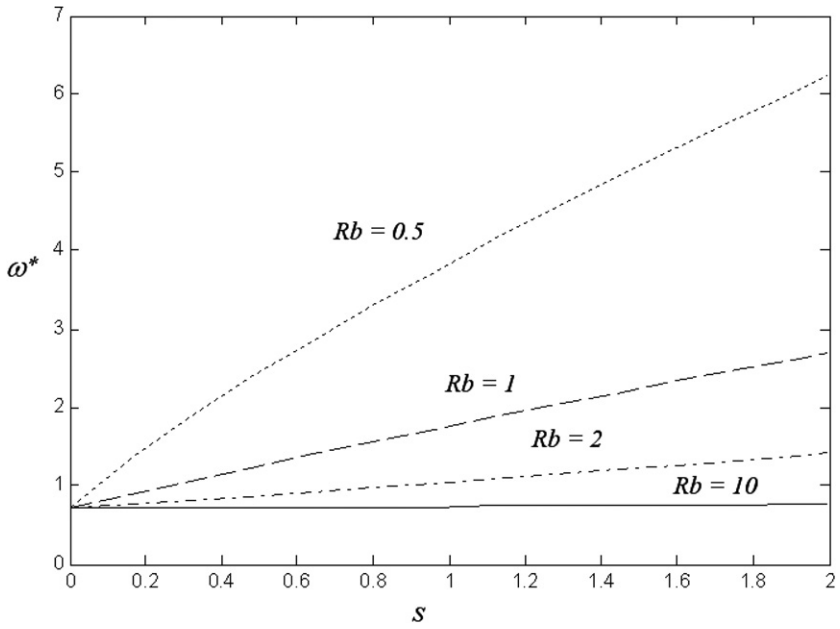

Figure 4. The plot shows the frequency of the most unstable mode, ω^*, as a function of arclength, s, for various Rossby numbers ($\mathcal{R}e_\alpha = 40$, $We = 20$, $\alpha = 0.8$).

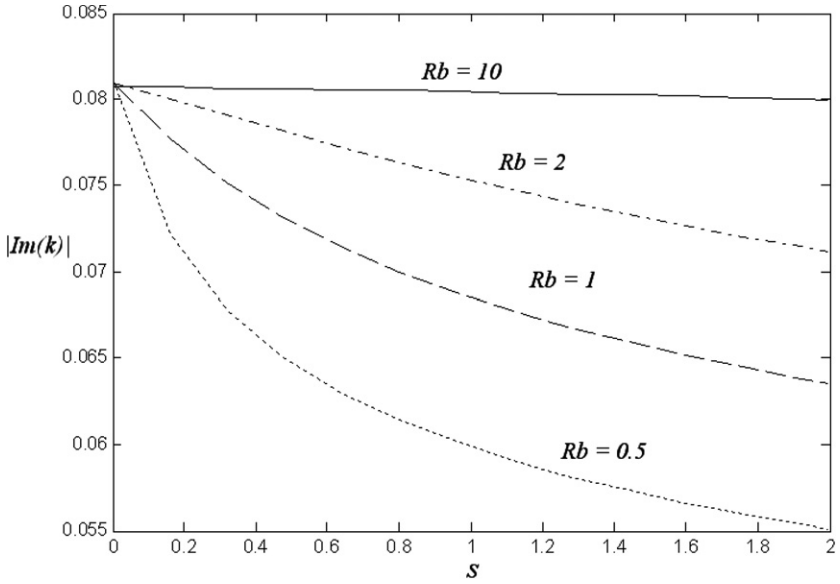

Figure 5. The plot shows the modulus of the growth rate, $|Im(k)|$, as a function of arclength, s, for various Rossby numbers ($\mathcal{R}e_\alpha = 40$, $We = 20$, $\alpha = 0.8$).

radius, $a = 0.001$ or 0.0015 m, was located on the cylinder wall, 50 mm from the vessel base. Both the aspect ratio and radius of the orifice are controlled experimental parameters which

Table 1. Properties of liquid systems.

	Liquid		
	0.1% CMC	0.2% CMC	0.3% CMC
Density (ρ) (kg m^{-3})	1025.05	1025.55	1026.99
Surface tension (σ) (N m^{-1})	0.0700	0.0712	0.0717
Consistency index (k) (Pa s$^{\alpha}$)	0.012	0.060	0.199
Power-law exponent (α)	0.920	0.748	0.654
U (ms^{-1})	0.494–2.321	0.364–2.466	0.686–2.944
We	5.37–118.45	2.91–89.37	10.19–124.68
Rb	0.52–1.90	0.39–1.21	0.37–1.08
Oh	0.02026–0.02293	0.03038–0.04648	0.04603–0.07175
$\mathcal{R}e_{\alpha}$	70.15–372.88	11.64–95.40	9.18–43.51

influence the exit velocity of the jet. Full details of the apparatus are given in Partridge *et al* [25].

The rotation rate of the drum was varied from 30 to 300 revolutions per minute (rpm) ($\Omega = 3.14$–31.4 rad s^{-1}). The average exit velocity of the jet (assuming a small change in total fluid height, thus a constant hydrostatic head in the can [25]) was calculated from the volume change in the drum over a measured time interval. A summary of the experimental conditions used is given in table 1.

Images of the jets were obtained using a high-speed digital camera (Photron Fastcam Super 10k), recording at either 250 or 500 frames per second. The images were analysed using Image Pro Express software (Datacell Ltd, UK) to obtain the 2D trajectories of the jets in the plane of the image, the coherent length of the jets from the orifice to the point of break-up and the size distribution of the droplets produced. To enable statistical measures of the break-up lengths and drop sizes, at least 35 break-up lengths and 200 drop sizes were measured for each experimental condition [25].

The fluids chosen for the experiments were dilute aqueous solutions of carboxymethylcellulose, CMC (Blanose Aqualon, France), a cellulose derivative with time-independent shear-thinning rheological properties which are best fitted using the power-law model [26]. Three different concentrations of CMC (0.1%, 0.2% and 0.3% by weight) were used, with physical properties shown in table 1. Values of the consistency index, k, and flow index, α, were obtained by performing a steady-state shear ramp from $0.1 < \dot{\gamma} < 1000$ s^{-1} using a controlled stress rheometer (TA AR 1000, TA Instruments, USA) equipped with a 4 cm, 1° cone and plate geometry. Several previous studies have used dilute polymer solutions to successfully mimic power-law behaviour [11, 27]; however as an extra check, oscillatory tests were also performed. No regime was found where the storage modulus became a significant parameter and hence the flow behaviour appears to be viscous dominated under all observed experimental conditions.

Surface tension, σ, was measured using a DuNouy ring tensiometer and density, ρ, was measured using a density bottle. All measurements were repeated at least three times and the absolute errors were less than 5%.

The break-up length, $s = s_b$, is taken from the experimental measurements and non-dimensionalized with respect to the radius of the drum, s_0. The values of the steady-state radius, $R_0(s_b)$, velocity, $u_0(s_b)$, and apparent viscosity $\eta_0(s_b)$ are obtained from the solution

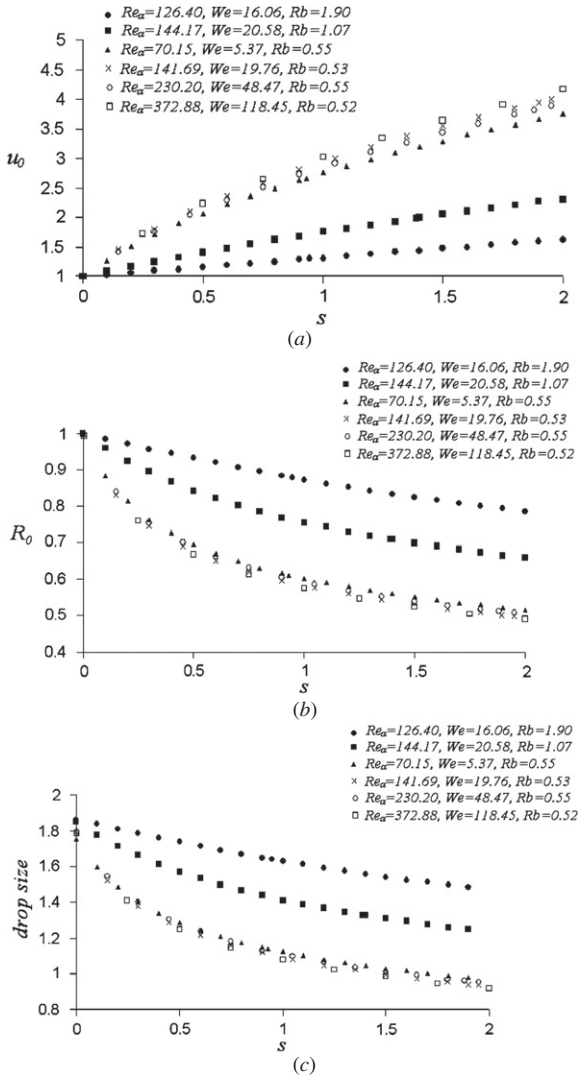

Figure 6. The plot shows (*a*) u_0, (*b*) the radius of the jet, R_0, and (*c*) the predicted drop radius, as a function of arclength, s, for various parameter values. For all solutions, $\alpha = 0.92$.

to the steady-state equations, which can be found in [3, 4] in addition to (3.26) and (3.25) . We then substitute $R_0(s_b)$, $u_0(s_b)$ and $\eta_0(s_b)$ into (4.3) adopting the view of spatial instability with $\lambda = -\mathrm{i}\omega$. The resulting equations are solved for k numerically for various values of ω to determine the most unstable wavenumber $k^*(s_b)$ as described in section 4. From this it is possible to determine the radius of the main droplet produced by this instability by calculating the volume of liquid in the wavelength at the break-up point. As these droplets will be approximately spherical, the main droplet radius can be determined from this volume. Equation (4.3) was solved computationally using real measured parameters from the experiments in order to determine the wavelength and hence the theoretical drop size at

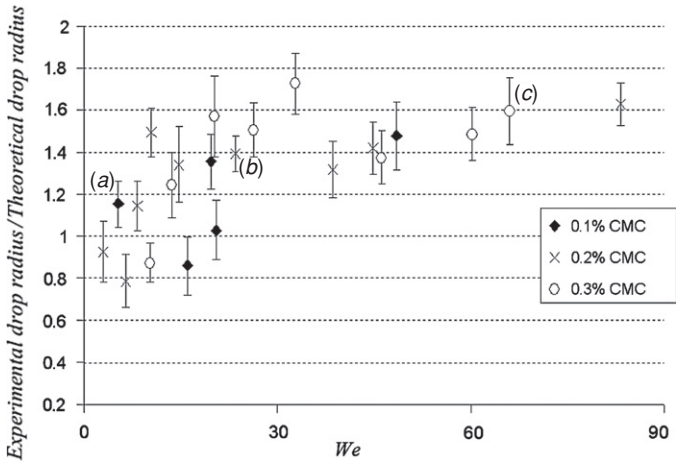

Figure 7. Experimental main drop radius/theoretical drop radius predictions for parameter sets as shown in table 2 plotted against the Weber number. Drop sizes are grouped by liquid system and the error bars represent the standard deviations given by the distribution of primary drop sizes obtained.

the experimental point of break-up. These results are then compared to drop sizes measured experimentally.

Figures 6(*a*), 6(*b*) and 6(*c*) demonstrate how u_0, the radius of the jet, R_0, and the predicted drop size vary with the arclength s in the computations for parameter values corresponding to experiments. The data presented in these graphs only present numerical predictions for 0.1% CMC, so $\alpha = 0.92$. The same trends are observed for 0.2% CMC and 0.3% CMC.

Figure 6(*b*) shows that the radius of the jet thins as it leaves the orifice. It can also be seen that Rossby number appears to have a greater impact on the rate at which the jet thins than the other experimental parameters. The predicted droplet radius, shown in figure 6(*c*), indicates how that parameter would vary if the jet breaks at different lengths, s. Thus, if the jet were longer, then the drops would be smaller.

The theoretical drop radii estimated using (4.3) are given in table 2 along with the experimental results and parameters examined. All the drop radii are normalized with respect to the radius of the orifice, a. The value of the break-up length is taken from the experimental observation.

The accuracy of the drop radii predictions is illustrated in figure 7. It can be seen from figure 7, where the theoretical value of the radius is compared to the experimental mean of the primary drop radii, that reasonable agreement between drop sizes acquired experimentally and theoretically is obtained. The results suggest that over the range of Weber numbers treated, the theory under-predicts the droplet radius, more than it over-predicts it and there appears to be some correlation between the Weber number and accuracy of the prediction. As the Weber number increases, the prediction of the droplet radius becomes less accurate.

Experimental images of the jet as the Weber number increases are shown in figure 8 and correlate to the points marked (*a*), (*b*) and (*c*) in figure 7. As the Weber number increases, these images show that the jet break-up becomes more complicated. At low Weber numbers (corresponding to low exit velocities) the jet is fairly straight-forward as demonstrated in figure 8(*a*). As the Weber number increases, so does the Reynolds number and jet break-up becomes more complicated. As can be seen in figures 8(*b*) and 8(*c*), the jet becomes

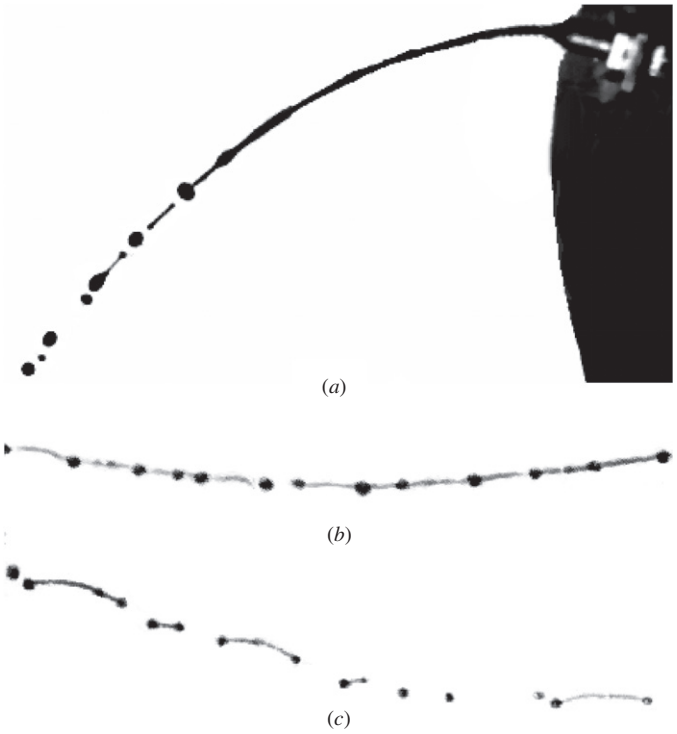

Figure 8. Experimental images of the jet (*a*) $We = 5.37$, $Rb = 0.552$, $Oh = 0.0229$, $\mathcal{R}e = 101.00$, $\rho = 1025\,\mathrm{kg\,m^{-3}}$, $k = 0.012$ Pa s^n, $n = 0.920$; (*b*) $We = 23.50$, $Rb = 0.588$, $Oh = 0.0356$, $\mathcal{R}e = 136.11$, $\rho = 1026\,\mathrm{kg\,m^{-3}}$, $k = 0.061$ Pa s^n, $n = 0.748$ and (*c*) $We = 65.99$, $Rb = 0.473$, $Oh = 0.0519$, $\mathcal{R}e = 156.31$, $\rho = 1027\,\mathrm{kg\,m^{-3}}$, $k = 0.199$ Pa s^n, $n = 0.654$.

increasingly complex for increasing Weber number and it is more difficult to accurately predict drop size.

The computations predict that different drop sizes arise depending on where the jet breaks. Figure 6(*c*) shows the drop size that will arise for different break-up lengths, calculated using the steady-state and the eigenvalue relationship (4.3). The actual break-up length depends upon the size of the disturbance at the orifice. If we know the size of the disturbance at the orifice, then the theory can be used to predict the break-up length. Experimental work with known forced disturbances at the orifice will follow, but this paper concerns unforced jets where the size of the disturbance at the orifice is unknown. The results in table 2 are determined by experimentally observing the break-up length and using that value to feed into the computations to predict the resulting drop size. However, at high Weber number, figure 8(*c*) shows that determining the location of the break-up point experimentally is not straightforward; there is not always a unique break-up point, but the jet may break at several locations simultaneously. Moreover, while the Weber number at the orifice, which is the Weber number quoted throughout the paper, is high, if a local Weber number were to be calculated on the ligament, this would probably be quite small as the speed of the flow within the ligament (not relative to the orifice) will be quite different to the initial speed of the jet, U, and the radius of the ligament is much smaller than a. Therefore, the break-up in 8(*c*) may not be convective, but instead absolute.

Table 2. Table of normalized drop sizes for experiments and predictions using the numerical model.

k (Pa s$^{\alpha}$)	α	We	Rb	$\mathcal{R}e_{\alpha}$	Experimental value $\pm$ s.d.	Model prediction
0.012	0.92	16.06	1.90	126.39	1.434 ± 0.138	1.6707
0.012	0.92	20.58	1.08	144.17	1.389 ± 0.142	1.3523
0.012	0.92	5.37	0.55	70.15	1.341 ± 0.112	1.1622
0.012	0.92	19.76	0.53	141.69	1.305 ± 0.129	0.9623
0.012	0.92	48.47	0.55	230.20	1.423 ± 0.161	0.9615
0.060	0.748	6.46	1.21	19.16	1.252 ± 0.126	1.5921
0.060	0.748	8.34	0.69	22.49	1.376 ± 0.119	1.995
0.060	0.748	2.91	0.41	11.64	1.104 ± 0.144	1.1928
0.060	0.748	10.41	0.39	25.99	1.248 ± 0.115	0.8356
0.060	0.748	23.50	0.39	43.58	1.020 ± 0.085	0.7321
0.060	0.748	83.21	0.44	95.40	1.161 ± 0.103	0.713
0.060	0.748	14.60	1.10	27.33	1.993 ± 0.178	1.4856
0.060	0.748	38.37	0.89	49.72	1.584 ± 0.133	1.2015
0.060	0.748	44.63	0.65	55.39	1.325 ± 0.123	0.9341
0.199	0.654	10.19	0.38	9.18	1.154 ± 0.094	1.3213
0.199	0.654	13.54	1.08	9.73	1.833 ± 0.156	1.4754
0.199	0.654	26.32	0.75	15.14	1.632 ± 0.129	1.0835
0.199	0.654	60.21	0.59	18.80	1.407 ± 0.125	0.9472
0.199	0.654	20.17	0.66	12.77	1.699 ± 0.194	1.0826
0.199	0.654	32.74	0.56	17.69	1.529 ± 0.145	0.8854
0.199	0.654	46.23	0.49	21.83	1.173 ± 0.126	0.8551
0.199	0.654	66.00	0.47	28.04	1.345 ± 0.158	0.8428

7. Conclusions

The effect of apparent viscosity on the trajectory of a rotating, slender non-Newtonian liquid jet emanating from a small orifice has been examined by incorporating the effects of non-Newtonian power-law rheology into the existing steady-state equations derived by Wallwork *et al* [3]. Apparent viscosity only appears as a higher order (in ϵ) correction to the inviscid steady centreline.

A linear dispersion relation has been obtained that can be solved computationally to establish the behaviour of wave modes as they propagate along a curved liquid jet. As the arclength, s, increases, the growth rate decreases, and the wavenumber with the largest growth rate occurs for higher values of frequency, ω.

Experiments have been performed to determine the trajectory and break-up of slender liquid jets over a wide range of parameters, with measurements of break-up length and drop size being taken. The mean droplet radius produced by instability has been determined using the linear instability calculations and the experimental value of break-up which enables a comparison between experimental and theoretical work. Some good points of agreement have been obtained between theoretical and experimental measurements of the size of the drops produced by instability, particularly at lower Weber numbers. At higher values of the Weber number, break-up may be via absolute instability on the observed slender ligament: this will be the subject of future work. All the fluids were tested for viscoelastic effects; however, at

high Weber number the jet does appear less laminar and there is the possibility that at high Weber number the stresses the fluids are being subjected to are more severe than can be tested accurately in the rheometer, particularly near break-up. It would be interesting to extend this work using the Olroyd-B model to see if there is any hint of viscoelasticity in the experimental results.

Acknowledgments

Victoria Hawkins was funded by an EPSRC studentship with the School of Chemical Engineering, University of Birmingham. The pilot scale experimental rig was developed as part of an EPSRC grant GR/R21349.

References

[1] Andersen K G and Yttri G 1997 Et forsøk verdt. Universitets for laget Oslo
[2] Ornek D, Gurkan T and Oztin C 2000 *J. Chem. Technol. Biotechnol.* **75** 689–94
[3] Wallwork I M, Decent S P, King A C and Schulkes R M S M 2002 *J. Fluid Mech.* **459** 43–65
[4] Decent S P, King A C, Simmons M J H, Părău E I, Wallwork I M, Gurney C J and Uddin J 2009 *Appl. Math. Modelling* **33** 4283–302
[5] Bousfield D W, Keunings R and Marucci G 1986 *J. Non-Newton. Fluid Mech.* **21** 79–97
[6] Li J and Fontelos M A 2003 *Phys. Fluids* **15** 922–36
[7] Clasen C, Eggers J, Fontelos M A, Li J and McKinley G H 2006 *J. Fluid Mech.* **556** 283–308
[8] McKinley G H 2005 *Annu. Rheol. Rev.* **3** 1–45
[9] Doshi P, Suryo R, Yildirim O E, McKinley G H and Basaran O A 2003 *J. Non-Newton. Fluid Mech.* **113** 1–27
[10] Eggers J 1993 *Phys. Rev. Lett.* **71** 3458–60
[11] Dravid V, Loke P B, Corvalan C M and Sojka P E 2008 *J. Fluids Eng.* **130** 081504
[12] Balmforth N J, Craster R V and Toniolo C 2003 *Phys. Fluids* **15** 3370–84
[13] Hwang C, Chen J, Wang J and Lin J 1994 *J. Phys. D: Appl. Phys.* **27** 2297–301
[14] Coronado Matutti O, Souza-Mendes P R and Carvallo M S 2004 *J. Fluids Eng.* **3** 386–90
[15] Berezin M P, Hutter K and Spodavara 1998 *Arch. Appl. Math.* **68** 169–78
[16] Uddin J, Decent S P and Simmons M J H 2006 *Trans. ASME, J. Fluids Eng.* **128** 968–75
[17] Uddin J, Decent S P and Simmons M J H 2008 *Int. J. Eng. Sci.* **45** 1253–65
[18] Rayleigh J W S 1878 *Proc. Lond. Math. Soc.* **10** 4–13
[19] Weber C 1931 *Z. Agnew. Math. Mech.* **1** 136–41
[20] Keller J B, Rubinow S I and Tu Y O 1973 *Phys. Fluids.* **16** 2052–5
[21] Nayfeh A H 1970 *Phys. Fluids.* **13** 841–7
[22] Părău E I, Decent S P, King A C, Simmons M J H and Wong D C 2006 *Wave Motion* **43** 599–618
[23] Hawkins V L 2009 *PhD Thesis* University of Birmingham
[24] Partridge L 2006 *PhD Thesis* University of Birmingham
[25] Partridge L, Wong D C Y, Simmons M J H, Părău E I and Decent S P 2005 *Chem. Eng. Res. Des.* **83** 1267–75
[26] Schowalter W R 1978 *The Mechanics of Non-Newtonian Fluids* (Oxford: Pergamon)
[27] Kitamura Y and Takahashi T 1982 *Can J. Chem. Eng.* **60** 732–7